Nuclear Instruments and Methods in Physics Research A 622 (2010) 246–255

Contents lists available at ScienceDirect

Nuclear Instruments and Methods in Physics Research A

journal homepage: www.elsevier.com/locate/nima

The effect of scintillator response on signal difference to noise ratio in X-ray medical imaging

K. Ninos, D. Cavouras, G. Fountos, I. Kandarakis *

Department of Medical Instruments Technology, Technological Educational Institution of Athens, 122 10 Athens, Greece

ARTICLE INFO

Article history:
Received 23 August 2009
Received in revised form
12 June 2010
Accepted 14 July 2010
Available online 24 July 2010

Keywords:
Scintillators
Phosphor screens
Luminescence efficiency
Contrast
Noise
X-ray imaging

ABSTRACT

The aim of the present study was to examine the effect of scintillator material properties on the signal difference to noise ratio (*SdNR*) under X-ray imaging conditions. To this aim, *SdNR* was modelled in terms of scintillator material properties such as the quantum detection efficiency (QDE), the intrinsic energy conversion efficiency (ICE) and the light transmission efficiency (LTE). Scintillators were assumed to be in the form of scintillator layers (phosphor screens) with various thicknesses ranging from 70 to 110 mg/cm^2. Data on the X-ray absorption and optical properties of the scintillators were either calculated from tabulated data, i.e. X-ray attenuation coefficients for QDE estimation, or were obtained from previous experimental studies. It was found that in a wide range of X-ray tube voltages the Gd_2O_2S:Tb scintillator produced higher *SdNR* values, while the CsI:Tl scintillator was better at lower voltages (below 65 kVp). It was additionally verified that, in the range of X-ray diagnostic energies, *SdNR* increases with the thickness of the scintillator layer screen. In conclusion, *SdNR* may be critically affected by scintillator properties and, hence, it may be significantly improved by appropriately selecting the type and thickness of the phosphor screen to be integrated into an imaging system.

1. Introduction

Most radiation detectors used in X-ray imaging consist of an X-ray to light converter, i.e. scintillator/phosphor layer, coupled to an optical detector (photographic emulsion, photocathode, photodiode, etc.) [1–4]. The principal material properties to take into account in evaluating scintillators for X-ray radiographic detectors are: the X-ray quantum detection efficiency (QDE), the intrinsic radiation to light conversion efficiency (ICE), i.e. absorbed X-ray energy converted into light, and the light transmission efficiency (LTE) [5–7], expressing the fraction of light passing through the scintillator material. However, additional parameters, related to an image creation, such as noise, contrast and resolution have to be estimated when scintillators are to be incorporated into an imaging detector.

The aim of the present study was to investigate theoretically the effect of scintillator response on the signal difference to noise ratio (*SdNR*), often employed as an image quality metric in medical imaging [8,9]. An *SdNR* was expressed in terms of scintillator material properties such as QDE, ICE, LTE as well as in terms of the X-ray transmission properties of simple one-dimensional software phantoms, simulating parts of the human body and lesions of varying dimensions. The investigation was performed for various X-ray scintillators, including two of the most commonly used materials, namely Gd_2O_2S and CsI.

To our knowledge the effects of scintillator properties on X-ray imaging *SdNR*, in the energy range, used in general radiography and fluoroscopy, have not been previously systematically studied.

2. Materials and methods

2.1. Model for output signal

The output signal of a scintillating screen was expressed by the emitted light photon fluence—Φ_Λ(light photons per unit of area) [11]

$$\Phi_\Lambda(E_0) = \int_0^{E_0} \phi_0(E)\eta_Q(E)m_\lambda(E)g_\Lambda(E,\sigma_0,\tau_0)\,dE \quad (1)$$

where $\phi_0(E)$ is the incident X-ray photon fluence spectral distribution (photon fluence per energy interval) [12,13]. E is the X-ray photon energy and E_0 is the maximum energy of the X-ray spectrum. $\eta_Q(E)$ is the quantum detection efficiency (QDE), being the fraction of the total number of incident X-ray quanta interacting in the scintillator. $m_\lambda(E)$ is the intrinsic quantum conversion gain, i.e. the number of light quanta generated within the scintillator per X-ray absorbed. g_Λ is the light transmission efficiency, expressing the fraction of light escaping the scintillator. This fraction may be described in terms of optical attenuation

* Corresponding author. Tel.: +30 210 5385387.
E-mail address: kandarakis@teiath.gr (I. Kandarakis).

0168-9002/$ - see front matter © 2010 Elsevier B.V. All rights reserved.
doi:10.1016/j.nima.2010.07.045

coefficients, σ_0 and τ_0 in (1), corresponding to optical absorption and scattering [14,15]. The light photon fluence was modelled by suitably modifying previously published theoretical models [5,10,11,14]. Details on the specific expressions and calculations of all the aforementioned quantities are given in Appendix and in Refs. [5,7,14].

2.2. SdNR model

To model *SdNR*, we have considered typical X-ray exposure situations as shown in Fig. 1. A parallel X-ray photon flux $\Phi_0(E)$ is incident on a phantom. The latter contains two different regions with different thicknesses (Fig. 1(a)) or different attenuation coefficients μ_1 and μ_2 (Fig. 1(b) and (c)). Once the X-ray flux exits the phantom region, it enters the scintillator (phosphor screen). The latter converts absorbed X-rays into light, and thus the final optical signal (Φ_1, Φ_2 in Fig. 1) is created and emitted. Under these conditions, the signal difference to noise ratio (*SdNR*) can be defined as follows

$$SdNR = \frac{\Delta\overline{\Phi}}{\sqrt{\sigma^2(\Delta\Phi)}}$$

where Φ denotes emitted light flux, σ is the standard deviation in light flux (Φ) values and the mean signal difference $\Delta\overline{\Phi}$ is written as

$$\Delta\overline{\Phi} = \Phi_1 - \Phi_2$$

$\Phi_i, i=1,2$ is the light flux emitted by the scintillator, corresponding to the two areas of the irradiated phantom projected on the scintillator screen surface (see Fig. 1(a)–(c)). The variance (standard deviation squared) of the signal difference is written as

$$\sigma^2(\Delta\Phi) = \sigma^2(\Phi_1) + \sigma^2(\Phi_2)$$

Finally, *SdNR* is expressed by the ratio

$$SdNR = \frac{\Phi_1 - \Phi_2}{(\sigma^2(\Phi_1) + \sigma^2(\Phi_2))^{1/2}} \quad (2)$$

Noise can then be expressed by the corresponding variances $\sigma(\Phi_1)$ and $\sigma(\Phi_2)$ in the denominator. The two signal levels, Φ_1 and Φ_2, exiting the corresponding two regions of the detector, where the incident X-rays are projected, may be written as follows

$$\Phi_1(E_0) = \int_0^{E_0} \phi_0(E,T_1(E))\eta_Q(E)m_{\lambda}(E)g_{\Lambda}(E,\sigma_0,\tau_0)dE \quad (3a)$$

$$\Phi_2(E_0) = \int_0^{E_0} \phi_0(E,T_2(E))\eta_Q(E)m_{\lambda}(E)g_{\Lambda}(E,\sigma_0,\tau_0)dE \quad (3b)$$

where $\phi_0(E,T_i(E))$ indicates the X-ray photon fluence exiting the two regions of the phantom, $T_i(E), i=1,2$ being the X-ray transmission functions expressing the attenuation of the X-ray beam transmitted through the two phantom regions.

$$T_1(E) = \exp[-\mu_1(E)L] \quad (4a)$$

$$T_2(E) = \exp\left[-\sum_i \mu_i(E)L_i\right] \quad (4b)$$

where L is the total thickness of the phantom, particularly the thickness of the first region (left part), consisting of a homogeneous material of constant thickness (see Fig. 1). μ_1 is the attenuation coefficient of this material. Eq. (4b) describes the attenuation of the X-ray beam through the second part of the phantom. This region of the phantom may consist of

(i). a thinner layer (step) of the same material (Fig. 1(a)), where

$$\sum_i \mu_i L_i = \mu_1 L_0, \quad L_0 \le L \quad (4c)$$

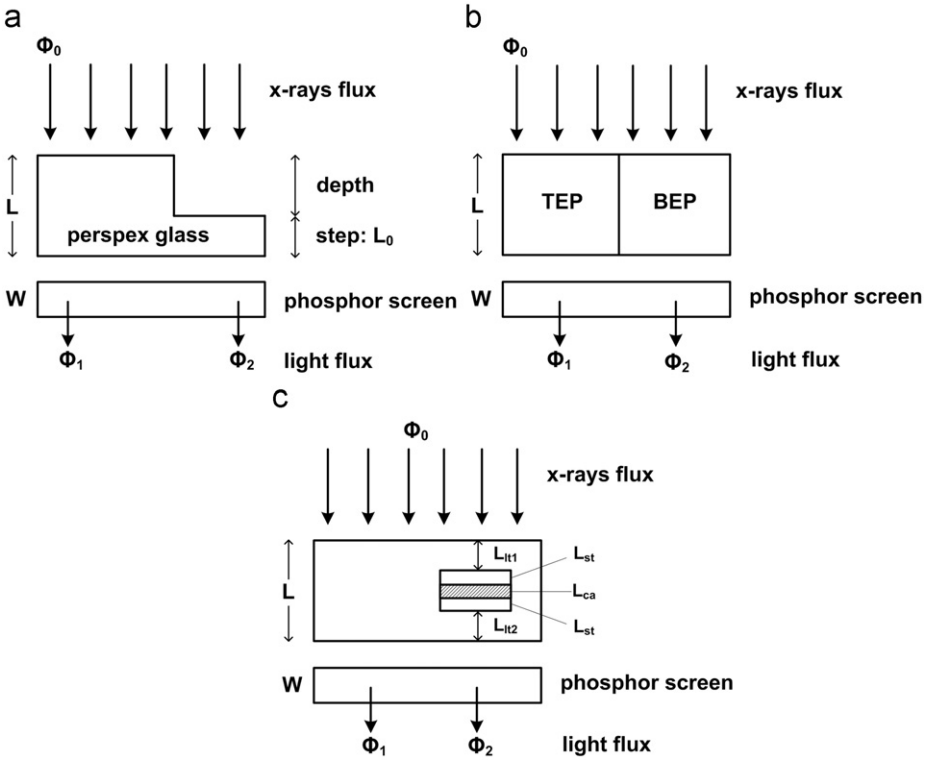

Fig. 1. (a) Perspex phantom of two steps: the thickness of the second step (L_0) was assumed to vary corresponding to various depths (4–14 cm) from the phantom surface. (b) Phantom consisting of two parts of different materials (BEP: Bone Equivalent Phantom, TEP: Tissue Equivalent Phantom) and equal thickness. (c) Perspex phantom of constant thickness containing a nodule.

(ii). a layer of equal thickness, however consisting of different material (Fig. 1(b)), where

$$\sum_i \mu_i L_i = \mu_2 L \tag{4d}$$

μ_2 being the attenuation coefficient of the material in the *right* region of the phantom in Fig. 1(b).

(iii). five superimposed layers as shown in Fig. 1(c), where

$$\sum_i \mu_i L_i = \mu_{lt} L_{lt1} + (\mu_{st} L_{st1} + \mu_{ca} L_{ca} + \mu_{st} L_{st2}) + \mu_{lt} L_{lt2} \tag{4e}$$

where the index *lt* stands for *lung tissue*, *st* stands for *soft tissue* and *ca* stands for *calcium tissue.*

The corresponding variances can be written as [16,17]

$$\sigma^2(\Phi_1) = \int_0^{E_0} \phi_0(E,T_1(E))\eta_Q(E)(m_\lambda(E)g_\Lambda(E,\sigma_0,\tau_0))^2\,dE \tag{5a}$$

$$\sigma^2(\Phi_2) = \int_0^{E_0} \phi_0(E,T_2(E))\eta_Q(E)(m_\lambda(E)g_\Lambda(E,\sigma_0,\tau_0))^2\,dE \tag{5b}$$

These equations have been previously derived [16,17] by considering that the quantities ϕ, m, η, g_Λ, are stochastic variables independent of each other. ϕ_0 and m_λ follow Poisson statistical distributions, while η_Q and g_Λ are expressed by binomial distributions.

Details for calculations and experimental methods are described in Appendix and in Refs. [5,7,18,19].

3. Results and discussion

The model of *SdNR* was used to test various scintillator materials, such as Gd_2O_2S:Tb, Gd_2O_2S:Eu, CsI:Tl, La_2O_2S:Tb and LSO:Ce (Lu_2SiO_5:Ce). Fig. 2 shows the variation of *SdNR* with X-ray tube voltage considering a 100 mg/cm^2 Gd_2O_2S:Tb screen and a two step phantom of 20 mm total Perspex thickness (as depicted in Fig. 1(a)). This thickness is within values often used in simulations of X-ray beam attenuation by an average human body [20]. The thickness of the second step was assumed to vary corresponding to various depths from the phantom surface. The depth of the second step (i.e. L–L_0 in Fig. 1(a)) varies from 4 to 14 cm. An *SdNR* increases with increasing step depth since the difference ($\Phi_1-\Phi_2$), in the numerator of Eq. (2), becomes larger due to the corresponding decreasing X-ray attenuation in the second step (see Eqs. (4b) and (4c) for T_2). As it can also be seen an *SdNR* increases slightly with increasing X-ray tube voltage, up to 80 kVp, and decreases at higher voltages, from 90 to 140 kVp. This type of variation may be attributed to a combination of effects related to the intrinsic properties of the particular phosphor (Gd_2O_2S) as well as to the inherent absorption and contrast properties of the phantom material. The simple SNR curve, calculated for a 20 cm Perspex glass without step (i.e. considering $\Phi_2=0$ in Eq. (2)), is shown between curves corresponding to 4 and 6 cm depths. SNR is not necessarily always higher than an *SdNR*, since the value of SNR is highly dependent on the thickness of the absorber (i.e. the thickness of the perspex glass). For instance, a very thick glass will absorb most of the X-rays incident on its surface and, thus, will result in a very small value of an SNR. However, this thick absorber next to a thinner one (i.e. in the shape of the step glass phantom assumed in this study) will most likely provide a high *SdNR* value. This is due to the high difference between the numbers of photons exiting the two absorbers.

To demonstrate the influence of the phosphor material properties, OQG (optical quantum gain: number of emitted light photons per incident X-ray) was taken into consideration. Fig. 3 shows the variation of OQG with tube voltage for several scintillator materials. OQG was calculated as Φ/N, where N is the integral of the X-ray spectrum and $\Phi=\Phi_1$ (see Fig. 1). The gain of all scintillators increases with increasing tube voltage. However, each material shows slightly different response; e.g. one may note that above about 95 kVp, the Gd_2O_2S:Tb phosphor shows higher quantum gain values than the rest of the scintillator materials. In the range of lower voltages, CsI:Tl is better. Gd_2O_2S:Eu shows a similar response, but somewhat lower than that of Gd_2O_2S:Tb. To examine the effects of the inherent X-ray absorption properties of the phantom (or tissue) material, the corresponding output contrast was estimated (see Fig. 4). The latter was calculated as $((\Phi_1-\Phi_2)/\Phi_1)$ [20]. Contrast decreases continuously with tube voltage, since it is principally affected by the inherent X-ray transmission properties of the phantom material. These properties are strongly affected by the X-ray attenuation coefficients, which decrease with the photon energy. A variation similar to that shown in Fig. 2, is observed in Fig. 5. This figure

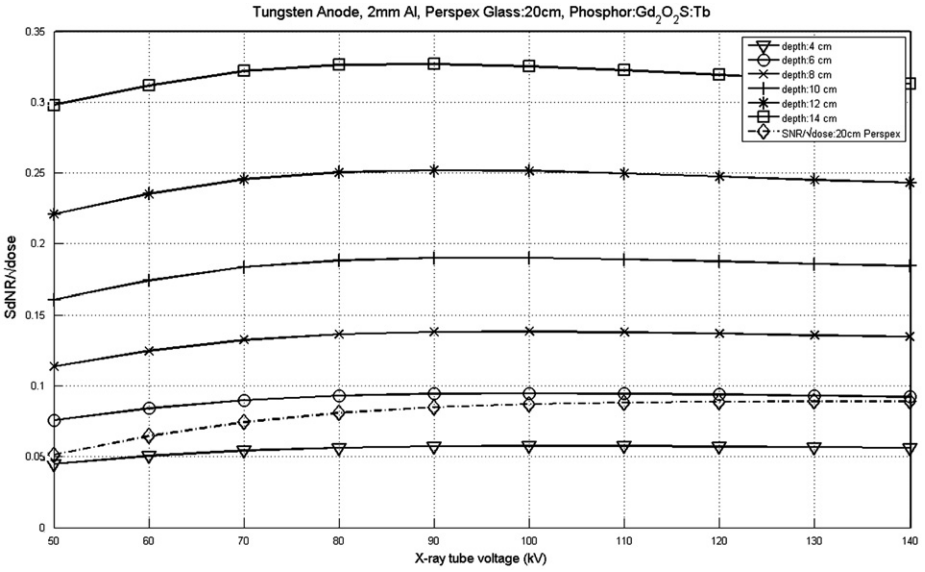

Fig. 2. Variation of an *SdNR* with kV, for different step depths of the phantom, for a Gd_2O_2S:Tb phosphor screen of 100 mg/cm^2 coating weight.

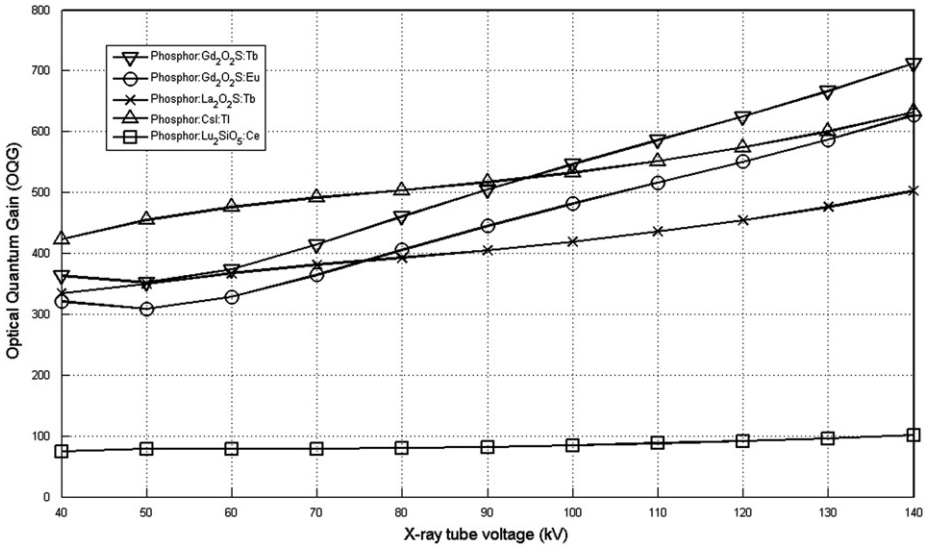

Fig. 3. Variation of optical quantum gain with X-ray tube voltage for various scintillators.

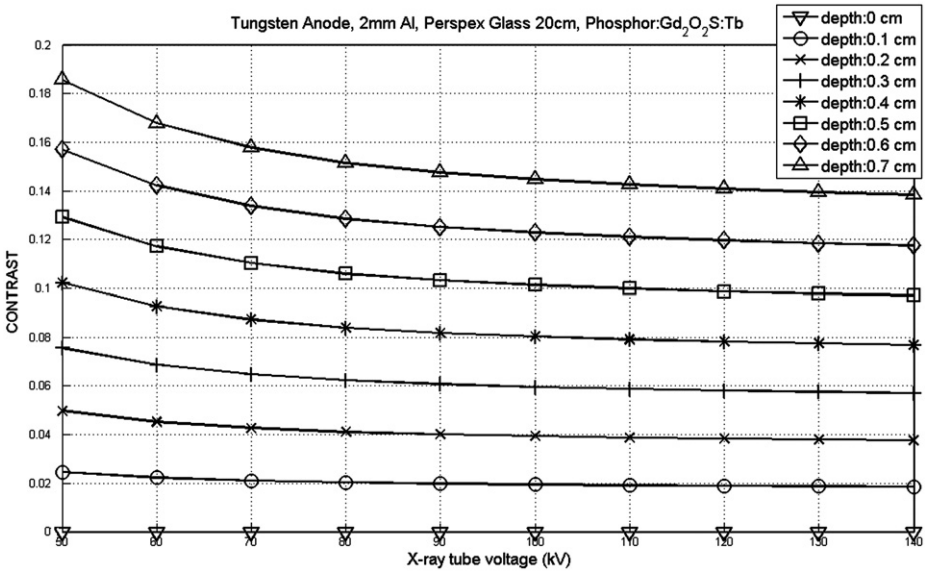

Fig. 4. Variation of contrast, for the Perspex phantom of two steps, with X-ray tube voltage.

depicts *SdNR* curves for various screen coating thickness, from 70 to 110 mg/cm^2, showing that thick screens produce higher *SdNR* values, apparently due to the higher X-ray absorption efficiency and higher quantum gain of thick screens, which produce higher amounts of light photons (Φ). However it is worth to note that, as it has been shown in previous studies [5,10,11], for a given powder scintillator material, light spreading, and hence image resolution is degraded with an increasing screen thickness [5,10,11].

All data shown in the figures are produced under the assumption of normalized X-ray spectra. Such spectra were determined according to a method described by Boone et al. [12] and are shown in Fig. 6. The X-ray tube voltage (and the corresponding maximum photon energy) increases up to 140 kVp; however, the total area under the spectral curve is equal for all spectral shapes.

Figs. 7 and 8 show *SdNR* curves for five different scintillator-phosphor materials, namely Gd_2O_2S:Tb, Gd_2O_2S:Eu, La_2O_2S:Tb, CsI:Tl and LSO:Ce (Lu_2SiO_5:Ce), considering variation of the *SdNR* with X-ray tube voltage for phosphors of 120 mg/cm^2 screen thickness (see Fig. 7) and variation of the *SdNR* with screen coating thickness at 100 kV X-ray tube voltage (see Fig. 8). As it can be observed from Fig. 7, for X-ray tube voltages higher than 65 kVp, the Gd_2O_2S phosphor was found to produce clearly higher *SdNR* values, particularly in the range of X-ray voltages above 90 kVp, Gd_2O_2S:Tb was more than 30% higher than CsI:Tl. For lower voltages, which also are employed in many radiographic techniques, the CsI:Tl phosphor seems to give better *SdNR* values. However, it is of interest to note that relatively high *SdNR* values are shown at very low voltages (e.g. 40 kVp) for the LSO:Ce phosphor. To go deeper into the effects of scintillators behaviour, we can comment on the following intrinsic properties of the scintillator materials:

(i). QDE: Gd_2O_2S shows high X-ray absorption efficiency within a wide spectrum of X-ray energies and particularly in the energy range above 50 keV, i.e. the energy of the *K*-absorption edge of Gd. In this range, the efficiency of the Gd_2O_2S phosphor increases with X-ray tube voltage,

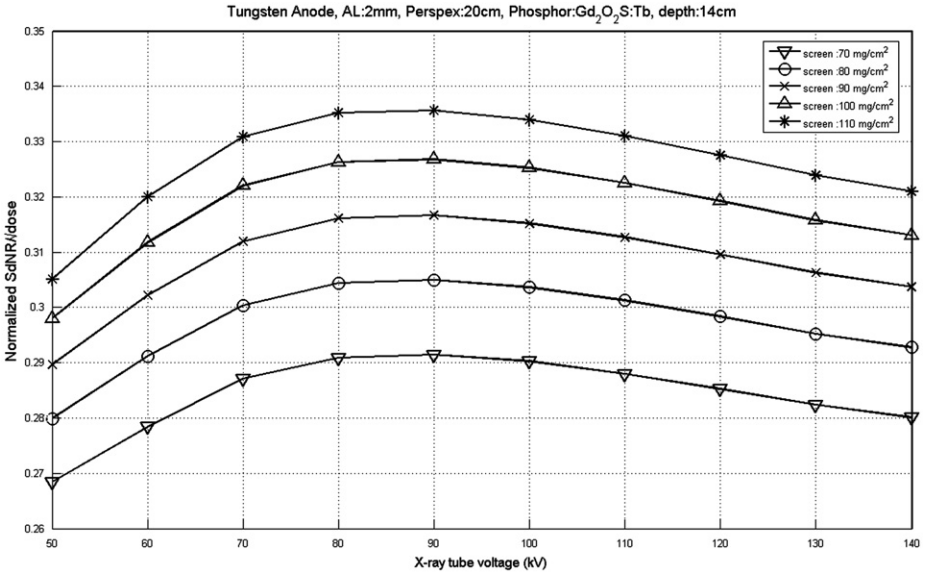

Fig. 5. *SdNR* curves for various screen coating thickness, from 70 to 110 mg/cm^2.

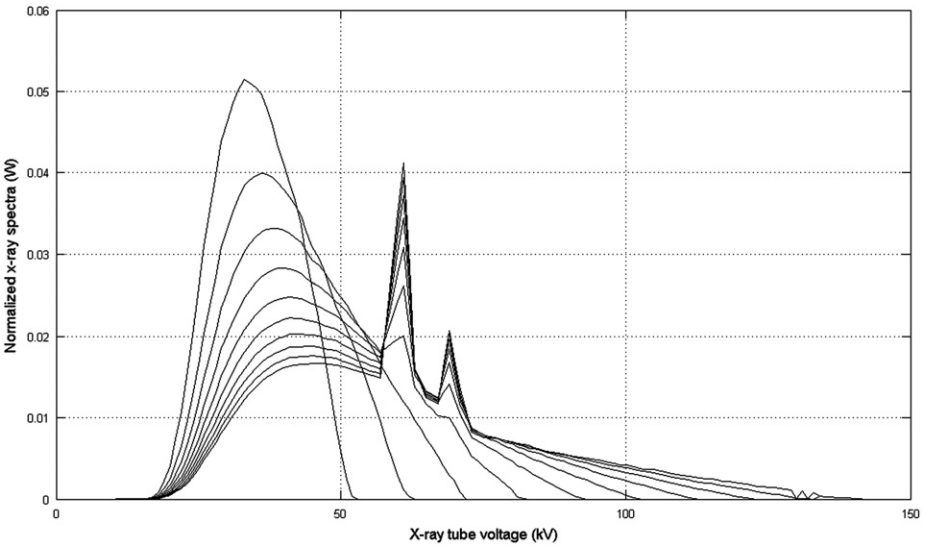

Fig. 6. Normalized X-ray spectra for various X-ray tube voltages.

since the fraction of the X-ray photon spectrum, exceeding the energy of 50 keV, becomes gradually larger at voltages higher than 50 kVp. In addition, Gd_2O_2S is a dense phosphor with high effective atomic number, which increases the probability of photoelectric absorption in the whole range of the diagnostic X-ray energies. On the other hand, CsI shows higher absorption at lower energies probably, due to its lower *K*-absorption edge energy (36 and 33.2 keV for Cs and I, respectively). Similar considerations may explain the lower absorption of La_2O_2S:Tb. Table 1 shows absorbed fractions of X-rays for each scintillator at an intermediate energy, e.g. 80 kVp. The smallest and largest scintillator thicknesses, converted to micrometers are also shown as well as the corresponding phosphor packing density, which is 50% of the nominal volume density for granular scintillators and 75% for CsI.

(ii). ICE: Gd_2O_2S:Tb shows higher intrinsic energy conversion efficiency than the other materials under consideration. This is mainly due to the small band-gap between the conduction and the valence bands of this material ($E_G=2.4$ eV, see Eq. (A3) in Appendix). Thus the amount of energy required to raise electrons from the lower to the higher band, and produce scintillations is smaller in the case of Gd than in other materials (e.g. for LSO:Ce, $E_G=6.4$ eV). This band-gap is also adequately small for the La_2O_2S:Tb scintillator. By fitting Eq. (1) to experimental quantum gain data, it was found that the intrinsic energy conversion efficiency of Gd_2O_2S and La_2O_2S:Tb was equal and approximately 0.18, while for the CsI phosphor it was of the order of 0.10.

(iii). LTE (attenuation of light within the scintillator): this property is significant in most X-ray scintillators, which are used in the form of grains embedded within a binding material to form the phosphor screen. Optical scattering on these grains, which plays an important role in light attenuation, is probably more significant within the LSO:Ce scintillator, due to the higher frequency (blue wavelength region) of this material's emission spectrum.

Fig. 9 shows the variation of *SdNR* for a phantom consisting of two different parts: one of tissue equivalent material (TEP) and one

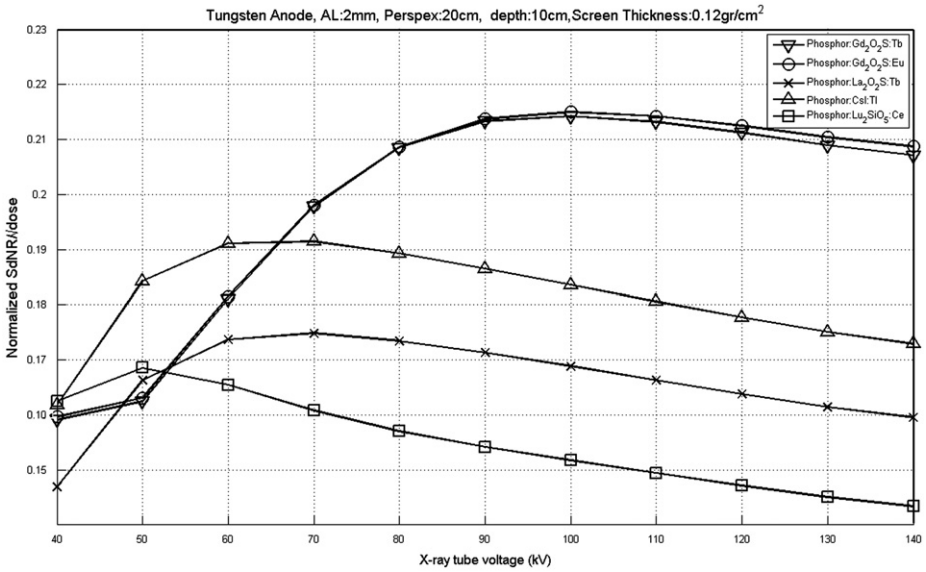

Fig. 7. Variation of *SdNR* with X-ray tube voltage for different phosphor materials considering 10 cm step depth.

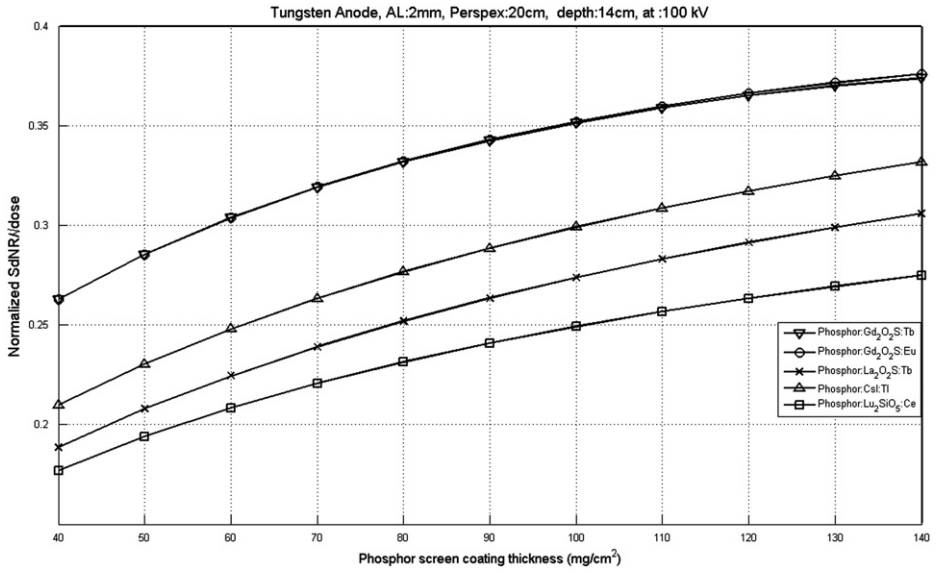

Fig. 8. Variation of *SdNR* with screen coating thickness for 14 cm step depth for different phosphor materials at 100 kV.

Table 1
Absorbed fractions, packing densities and scintillator corresponding to the smallest and largest coating thicknesses (40 and 140 mg/cm^2) at 80 kV X-ray tube voltage.

Scintillator	Scintillator packing density (g/cm^3)	Thickness for 40 mg/cm^2 coating weight (μm)	Thickness for 140 mg/cm^2 coating weight (μm)	QDE for screen of 40 mg/cm^2 coating weight	QDE for screen of 140 mg/cm^2 coating weight
Gd_2O_2S	3.67	108.99	381.47	0.35	0.73
La_2O_2S	2.81	142.35	498.22	0.18	0.49
CsI	3.82	104.58	366.01	0.22	0.56
Lu_2SiO_5	3.70	108.11	378.38	0.17	0.43

of bone equivalent material (BEP), of equal thickness (see Fig. 1(b)). A 100 mg/cm^2 Gd_2O_2S:Tb scintillator screen was assumed. *SdNR* varies as a function of X-ray tube voltage and as a function of phantom material thickness. Attenuation coefficients for these two materials were obtained from tabulated data [17,18]. *SdNR* decreases with increasing phantom thickness, since thick phantom (or human body) parts are penetrated by smaller number of X-ray photons, producing lower light flux at the detector. It is also of interest to note that, apparently due to X-ray beam hardening effects, the maximum *SdNR* shifts towards higher X-ray voltages as

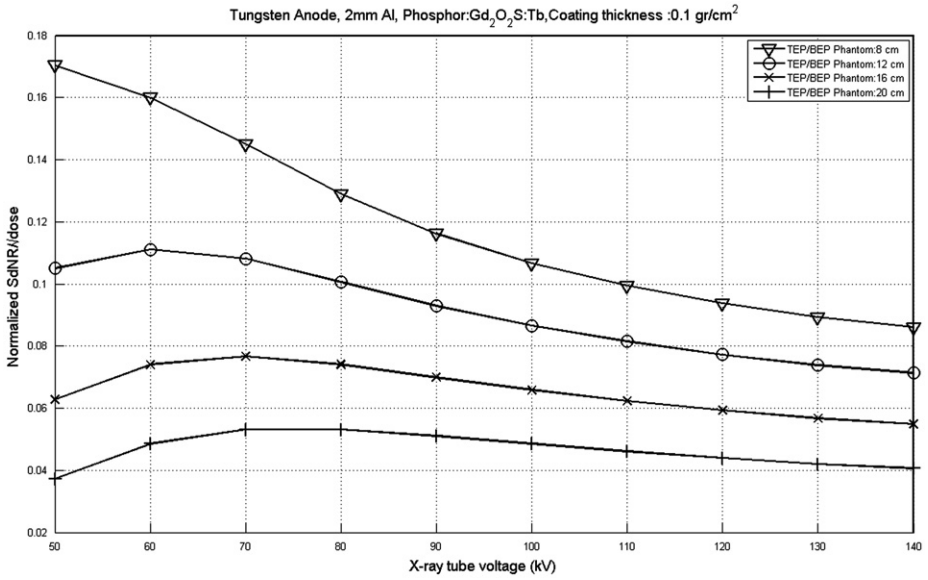

Fig. 9. Variation of *SdNR* with kV for Gd_2O_2S:Tb phosphor with 100 mg/cm^2 coating thickness and for various TEP/BEP phantom thicknesses (seeFig. 1(b)).

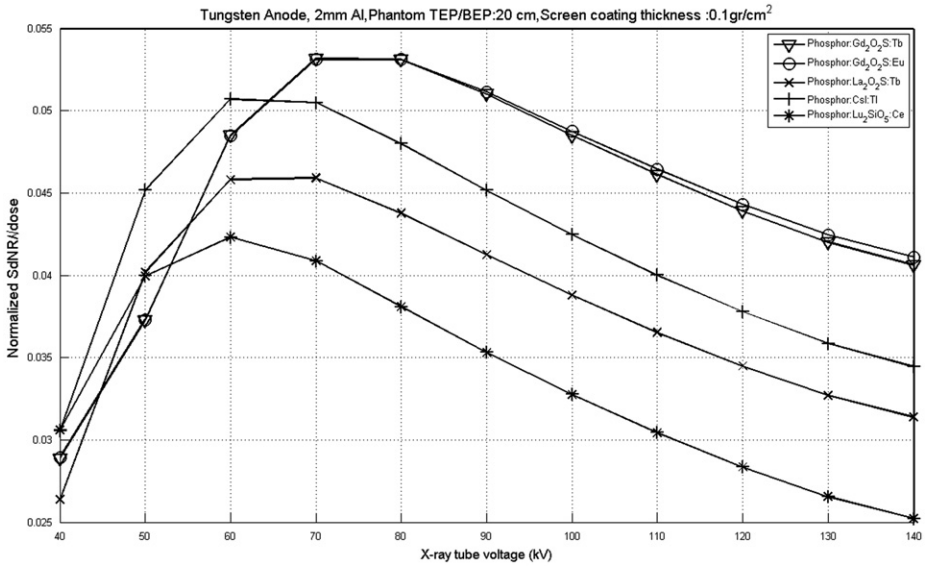

Fig. 10. Comparison between scintillator materials under the same irradiation conditions (20 cm TEP/BEP phantom thickness).

phantom thickness increases. A comparison between scintillator materials under the same irradiation conditions (20 cm TEP/BEP phantom thickness) is shown in Fig. 10. Gd_2O_2S:Tb (and Gd_2O_2S:Eu) shows again higher *SdNR* values in the voltage range after 65 kVp, while CsI is better at lower voltages. The rest of the scintillators were found with clearly lower *SdNR* values.

Figs. 11 and 12 show the *SdNR* data for a phantom, shown in Fig. 1(c), consisting of 20 cm of lung tissue containing a nodule of mixed tissue (2/8 calcium and 6/8 soft tissue). Nodule dimensions increase gradually from 1.1 to 5.1 cm. A shift of maximum *SdNR* towards higher voltages with increasing nodule dimensions is clearly shown. This is also explained by considering beam hardening effects. As shown in Fig. 12, Gd_2O_2S:Tb is always higher than the other materials in the range of voltages after 65 kVp. It is of interest to note that, in all cases, relatively high *SdNR* values were found at very low voltages (e.g. 40 kVp) for the LSO:Ce phosphor.

4. Summary and conclusion

In the present study, the effect of scintillator material's intrinsic properties on the performance of X-ray imaging systems was investigated by examining the signal difference to noise ratio. *SdNR* was modelled in terms of QDE, ICE and LTE using calculations based on data derived from light emission efficiency measurements. The X-ray absorption properties were estimated by calculations based on X-ray spectra and attenuation coefficients obtained from tabulated data. It was found that *SdNR* is clearly affected by the quantum gain of the scintillators, which in turn depends on QDE, ICE and LTE. The thickness of the phantom is also of concern, since its absorption properties affect the X-rays incident on the phantom and, hence, the scintillators' performance. The Gd_2O_2S:Tb phosphor gave highest *SdNR* values in a wide range of X-ray voltages, while CsI:Tl was better in the lower range of X-ray tube voltages below 65 kVp.

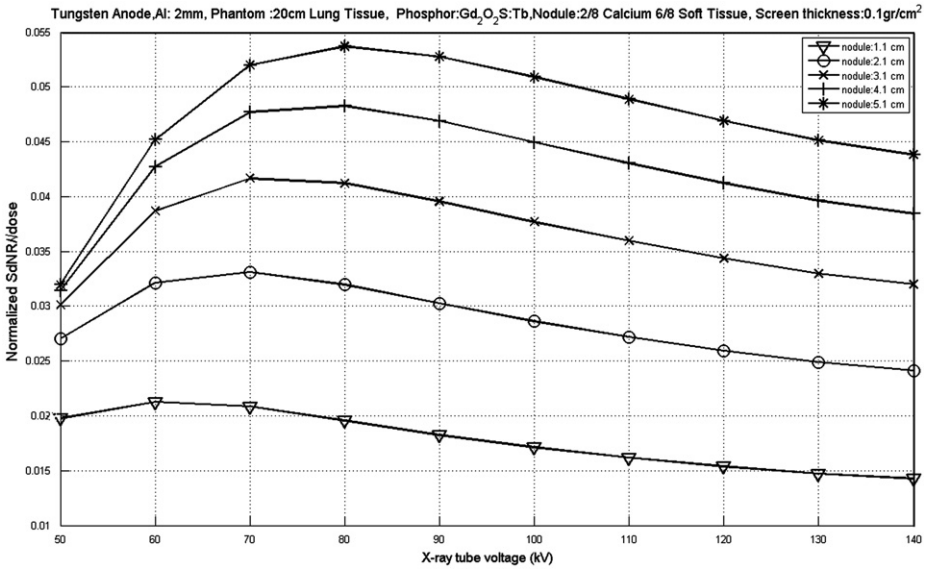

Fig. 11. *SdNR* data for a phantom consisting of 20 cm of lung tissue containing a nodule of 6/8 soft tissue and 2/8 calcium (see Fig. 1(c)).

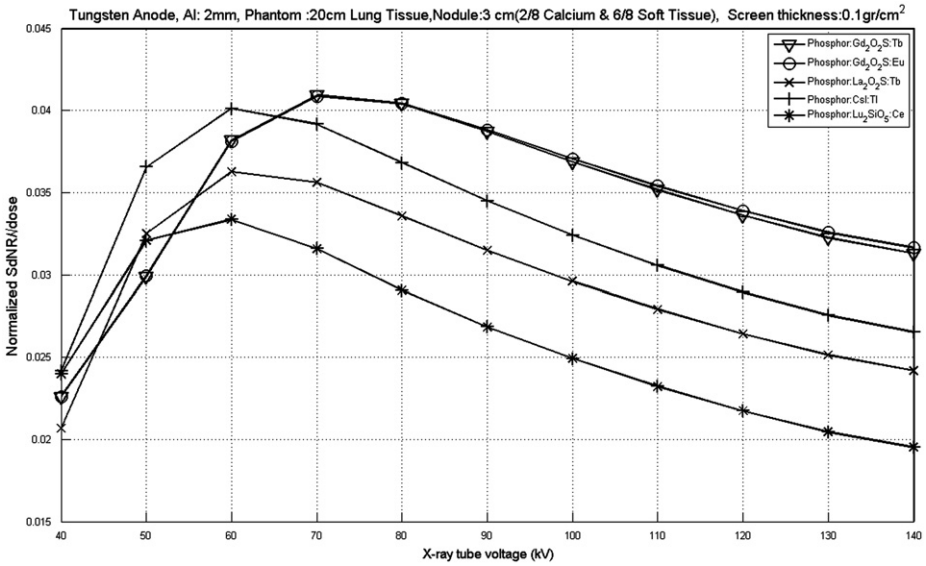

Fig. 12. Variation of *SdNR* for various scintillators, considering a phantom consisting of 20 cm of lung tissue containing a 2/8 calcium, 6/8 soft tissue nodule (see Fig. 3(c)).

Appendix

A1 Calculations and measurements

The parameters related to the incident X-ray flux and the intrinsic properties of the scintillators were estimated as follows:

1. The incident X-ray flux was determined as described in the previous studies [12,13].
2. The quantum detection efficiency was calculated by considering an exponential attenuation according to the law.

$$\eta_Q(E) = 1 - \exp\left[-\mu_s(E)w\right] \tag{A1}$$

where $\mu_s(E)$ is the X-ray attenuation coefficient of the scintillator and w is the coating thickness of the scintillator layer (screen).

3. The intrinsic quantum conversion gain was expressed as follows:

$$m_{\lambda}(E,\lambda) = \eta_C(E/h\nu) \tag{A2}$$

where η_C is the intrinsic energy conversion efficiency of the scintillator, expressing the fraction of absorbed X-ray energy that is converted into light within the scintillator and $h\nu$ is the mean energy of the emitted light photons. The maximum value of the intrinsic conversion efficiency was expressed as follows [1–3]:

$$\eta_C = (h\nu/\beta_0 E_G)SQ \tag{A3}$$

where $h\nu$ is the average energy of emitted light photons. $\beta_0 E_G$ represents the average energy that must be transferred by a fast electron (e.g. a photoelectron) to create an electron–hole pair in the scintillator. E_G is the forbidden energy band-gap

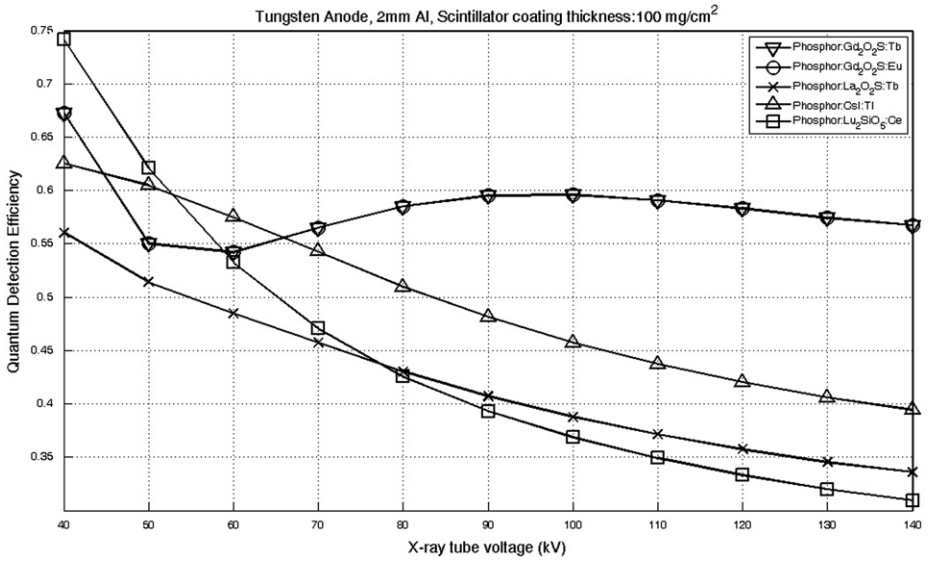

Fig. A1. Variation of the X-ray quantum detection efficiency with X-ray tube voltage, for the scintillators (100 mg/cm^2) investigate in this study.

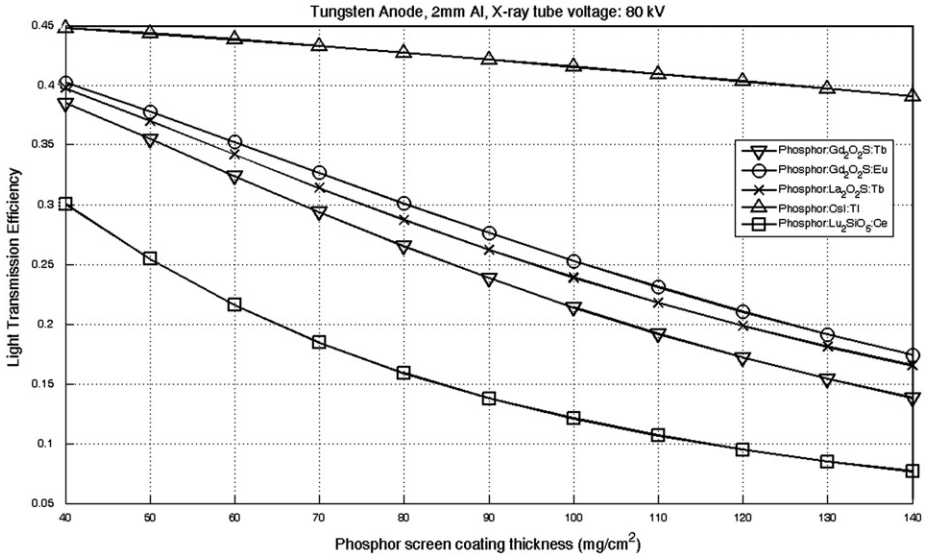

Fig. A2. Variation of the light transmission efficiency with screen coating thickness calculated for scintillators investigated in this study at 80 kVp.

between the valence and the conduction energy bands of the scintillator material [1–3]. β_0 is a parameter related to energy losses to lattice vibrations. S is the transfer efficiency with which electrons are transferred from the point of their creation to the luminescent centre (activator) and Q is the absorption efficiency of electrons at the luminescent centre [1–4]. In the present study, it was assumed $SQ=1$, corresponding to the maximum achievable value of the intrinsic conversion efficiency.

4. The light transmission efficiency, $\overline{g}_{\Lambda}(\sigma_0,\tau_0,\rho)$ in relation (1), of a scintillating screen may be expressed as follows:

$$g_{\Lambda}(E,\sigma_0,\tau_0,\rho)=\int_0^{w_0}\overline{\varphi}_X(E,w)\overline{g}_{\lambda}(\sigma_0,\tau_0,\rho,w)dwdE \tag{A4}$$

w_0 is the total screen thickness. For the purposes of analysis, it has been considered that the screen was divided into a large number of superimposed elementary thin layers of thickness Δw. Here, w denotes the depth of each thin layer from the screen surface. The function $\overline{\phi}_X(E,w)$ describes the relative probability of X-ray absorption at a depth w from the screen surface by the relation

$$\overline{\phi}_X(E,w)=\frac{\mu(E)\exp[-\mu(E)w]dw}{\int_0^{w_0}\mu(E)\exp[-\mu(E)w]dw} \tag{A5}$$

where $\mu(E)$ is the X-ray absorption coefficient calculated using tabulated data [18,19]. The numerator in Eq. (A5) gives the probability of X-ray photon absorption at depth w. The denominator is equal to the total probability of absorption in a scintillator of thickness w_0.

The function $\overline{g}_{\lambda}(\sigma_0,\tau_0,\rho)$ has been defined as a solution to the photon diffusion differential equation [5,14], describing light propagation through light scattering media:

$$\overline{g}_{\lambda}(\sigma_0,\tau_0,\rho_0)=\frac{\tau_0\rho_1[(\sigma_0+\tau_0\rho_0)e^{\sigma_0 w}+(\sigma_0-\tau_0\rho_0)e^{-\sigma_0 w}]}{(\sigma_0+\tau_0\rho_0)(\sigma_0+\tau_0\rho_1)e^{\sigma_0 w_0}-(\sigma_0-\tau_0\rho_0)(\sigma_0-\tau_0\rho_1)e^{-\sigma_0 w_0}} \tag{A6}$$

where σ_0 is the light attenuation coefficient of the scintillator, which is equal to the reciprocal of the light photon diffusion

length [5,14], and it is given as a function of the optical scattering coefficient(s), and the optical absorption coefficient (a), i.e. $\sigma_0=[a(a+2s)]^{1/2}$. τ_0 is the inverse relaxation length given as $\tau_0=a+2s$. ρ_0, ρ_1 are optical parameters expressing the reflection of light at the front and back scintillator surfaces: $\rho_n=(1-r_n)/(1+r_n)$, where r_n denotes the optical reflection coefficients at the front ($n=0$) and back ($n=1$) screen surfaces. In this study, we have used $\rho_0=0.91$, $\rho_1=0.87$ (obtained from previous studies [5,10,11]) and the values of σ_0 and τ_0 were found by fitting (see text). Eq. (A6) corresponds to the transmission mode. Plots showing the variation of quantum detection efficiency with X-ray tube voltage as well as the variation of the light transmission efficiency, $\overline{g}_A(\sigma_0,\tau_0,\rho)$ in relation (1), with screen thickness are shown in Figs. A1 and A2, respectively. The quantum detection efficiency decreases with X-ray tube voltage, due to the lower X-ray absorption and scattering at higher X-ray photon energies. Curve corresponding to the Gd_2O_2S:Tb powder scintillator shows an increasing part in the range 60–90 kVp, which is attributed to the influence of the K-absorption edge effect at 50 keV in the Gd atom of this material. The light transmission efficiency decreases with screen coating thickness, since light absorption and scattering effects become more important in thick screens. Light transmission was higher for the CsI:Tl scintillator and lower for LSO:Ce.

A2 Experiments

The scintillating screens were prepared in our laboratory by sedimentation of various phosphor powders on fused silica substrates (spectrosil B). Na_2SiO_3 was used as binding material between the powder particles. The coating thickness of the screens varied from approximately 70–110 mg/cm^2. The scintillating screens were irradiated by X-rays at various tube voltages (from 50 to 140 kV) employing a Philips Optimus X-ray radiographic unit. Tube filtration was 2.5 mm Al.

The experimental set-up for light energy fluence measurements comprised a photomultiplier (EMI 9798 B) with an extended sensitivity S-20 photocathode, and enclosed within a bronze light tight chamber. The photomultiplier current was amplified and fed to a vibrating reed (Cary 400) electrometer operated in the current mode. An analogue to digital converter was employed to digitise the electrometer's output, which was then stored on a computer.

The light flux was then computed from the electrometer's output current by performing conversions and corrections according to the formula

$$\eta_A=\frac{i_{elec}(pA)}{Sn_pc_sc_g} \tag{A7}$$

where i_{elec} is the electrometer's output current in pA. S is the area of an irradiated screen. n_p is the photocathode's peak photosensitivity expressed in mA/W. This was used as a factor for converting the output photocathode current into light power (light energy fluence). c_s is the spectral compatibility factor expressing the compatibility of the scintillator's emission spectrum to the spectral sensitivity of the photocathode (extended S-20) [15]. c_s was determined by the relation

$$c_S=\int \phi(\lambda)s(\lambda)d\lambda/\int s(\lambda)d\lambda \tag{A8}$$

where $\phi(\lambda)$ is the scintillator's emission spectrum and $s(\lambda)$ is the spectral sensitivity of the photocathode (known from the manufacturer's datasheet). This sensitivity was also verified in our laboratory, using a series of prototype LED light sources (Kingbright Co.) ranging from violet to red colour. The scintillator optical emission spectrum was measured during X-ray irradiation by an Ocean Optics S2000 grating spectrometer (Ocean Optics Inc.). c_g is the geometric light collection efficiency of the experimental set-up, expressing the fraction of the screen's light incident on the photocathode. This fraction has been determined by considering: (a) the angular distribution of light emitted by the screen and (b) the distance between the screen and the photocathode.

References

[1] H. Wieczorek, Radiat. Meas. 33 (2001) 541.
[2] C.W.E. van Eijk, Phys. Med. Biol. 47 (2002) R85–R106.
[3] G. Blasse, B.C. Grabmaier, in: Luminescent Materials, Springer-Verlag, Berlin, Heidelberg, 1994 p.85.
[4] C.W.E. van Eijk, Nucl. Instr. and Meth. Phys. Res. A 460 (2001) 1.
[5] I. Kandarakis, D. Cavouras, Nucl. Instr. and Meth. Phys. Res. A 460 (2001) 412.
[6] D. Cavouras, I. Kandarakis, M. Kanellopoulos, C.D. Nomicos, G.S. Panayiotakis, Appl. Radiat. Isot. 51 (1999) 59 ± 68.
[7] G.W. Ludwig, J. Electrochem. Soc. 118 (7) (1971) 1152.
[8] G. Patatoukas, A. Gaitanis, N. Kalivas, P. Liaparinos, D. Nikolopoulos, A. Konstantinidis, I. Kandarakis, D. Cavouras, G. Panayiotakis, Nucl. Instr. and Meth. Phys. Res. A 569 (2006) 260.
[9] M. Skarpathiotakis, M.J. Yaffe, A.K. Bloomquist, D. Rico, S. Muller, A. Rick, F. Jeunehomme, Med. Phys. 29 (2002) 2419.
[10] C. Michail, A. Toutountzis, S. David, N. Kalivas, I. Valais, I. Kandarakis, G. Panayiotakis, Appl. Phys. B (Lasers Opt.) 95 (2009) 131.
[11] S. David, C. Michail, I. Valais, A. Toutoutzis, P. Liaparinos, D. Cavouras, I. Kandarakis, G. Panayiotakis, IEEE Trans. Nucl. Sci. (TNS), TNS- 55 (2008) 3684.
[12] J.M. Boone, X-ray production, interaction, and detection in diagnostic imaging, in: J. Beutel, H.L. Kundel, R.L. Van Metter (Eds.), Handbook of Medical Imaging, vol. 1, Physics and Psycophysics, SPIE Press, Bellingham2000, p. 40.
[13] J.M. Boone, J.A. Seibert, Med. Phys. 24 (1997) 1661.
[14] R.K. Swank, Appl. Opt. 12 (8) (1973) 1865.
[15] P. Liaparinos, I. Kandarakis, D. Cavouras, H. Delis, G. Panagiotakis, Med. Phys. 34 (2007) 1724.
[16] I. Kandarakis, D. Cavouras, E. Kanellopoulos, C.D. Nomicos, G.S. Panayiotakis, Nucl. Instr. and Meth. Phys. Res. A 417 (1998) 86.
[17] R. Shaw, R. Van Metter, Proc. SPIE 454 (1984) 128.
[18] J.H. Hubbel, S.M. Seltzer, Tables of X-ray mass attenuation coefficients and mass energy absorption coefficients 1 keV to 20 MeV for elements $Z=1$ to 92 and 48 additional substances of dosimetric interest. U.S. Department of commerce. NISTIR 5632, 1995.
[19] E. Storm, H. Israel, Photon cross-sections from 0.001 to 100 MeV for elements 1 through 100, *Report LA-3753* Los Alamos Scientific Laboratory of the University of California, 1967.
[20] J.T. Dobbins, Image quality metrics for digital imaging, in: J. Beutel, H.L. Kundel, R.L. Van Metter (Eds.), Handbook of Medical Imaging, vol. 1, Physics and Psycophysics, SPIE Press, Bellingham2000, pp. 176–1177.